

*Review*

# Irradiance Variability Quantification and Small-Scale Averaging in Space and Time: A Short Review

Gerald M. Lohmann 

Energy Meteorology Group, Institute of Physics, Oldenburg University, Germany  
gerald.lohmann@uni-oldenburg.de

**Abstract:** With the continual global increase of PV power systems and the inherent weather-induced volatility of their power output, understanding the underlying variability of solar radiation in both space and time is important for the planning and reliable operation of future power grids. This paper concisely reviews recent advances in the characterization of irradiance variability with an emphasis on small spatial and temporal scales (respectively less than about 10 km and 1 min), for which comprehensive data sets are time consuming and expensive to collect, and although needed have not been available until recently. Special attention is given to studies dealing with the quantification of variability using such unique data, the analysis and modeling of spatial smoothing, and the evaluation of temporal averaging.

**Keywords:** irradiance variability, high-resolution measurements, increment statistics

---

## 1. Introduction

The installed capacity of photovoltaic (PV) power has noticeably increased in many regions of the world during the last decade, and it is expected to continue its recent fast-paced growth (e.g. 25 % in 2015 [1]). From well over 200 GW in the beginning of 2016 [2], the world-wide PV capacity is estimated to multiply more than tenfold until 2030, with capacity projections ranging between 3 TW and 10 TW [3]. As a consequence, the challenges associated with the intrinsic volatility of PV power production will considerably increase as well [4,5]. These challenges include the correct estimation of a PV system's yield [6], the proper dimensioning of energy storage [7], the balancing of generation and load [8], as well as the maintenance of power quality, such as voltage and frequency stability [9]. As PV power variability is primarily determined by weather-induced heterogeneity in solar irradiance fields [10], a comprehensive data-driven characterization of irradiance variability is key to the planning and reliable operation of future power grids and their corresponding subsystems.

Variability in both irradiance and irradiance increments (i.e., changes over specified intervals of time; a.k.a. changes [e.g., 11], step changes [e.g., 12], or ramp rates [e.g., 13]) are of interest in this context. Variability in irradiance itself primarily affects the yield of a PV system and the dimensioning of energy storage, while variability in irradiance increments impacts the balancing of generation and load as well as the maintenance of power quality. Depending on the dimensions of the power grid and PV capacity in question, relevant irradiance variability can span a broad range of spatiotemporal scales, from seconds and meters up to days and hundreds of kilometers [14]. There is an ongoing need to understand the biases in representation of temporal variability resulting from temporally coarse-resolution observations [15,16], as well as how spatial averaging (as would come from having distributed PV over a region) mitigates variability [17,18]. This is especially true for small sub-minute and sub-kilometer scales, which have only begun to receive increased scientific attention during the last couple of years, and for which comprehensive data sets are time consuming and expensive to collect, and although needed have not previously been available [10,11,14].

Early ground-based analyses have characterized single-site irradiance on time scales ranging from hours to months [19,20], while later studies have often been geared towards increasing temporal resolutions of, e.g., 300 s [21,22], 60 s [23–26], 20 s [11,27,28], 10 s [10,12,29], 5 s [30,31], 1 s [13,32–49],

and occasionally even down to 0.1 s [50], 0.04 s [51] and 0.01 s [15,16,52,53]. Yet, the spatial coverage of many of these data sets has remained very confined due to the typically small number of pyranometers in simultaneous operation. Satellite-derived irradiance data have additionally been used in order to augment the ground-based measurements and to extend the analyses to larger spatial scales on the order of tens of kilometers and more [10,28,54]. However, the best possible temporal resolutions realized by these satellite data range between about 15 min and 1 h. In one way or another, all studies have thus been either restricted to a limited spatial resolution, a limited temporal resolution, or both. Some studies have used artificially generated data to overcome these restrictions, either by simulating cloud shapes of varying complexity [40,55–58] and/or by constructing virtual networks based on time shifted single sensor measurements [11,12,58]. However, these simulated data do not necessarily coincide with reality. To remedy some of the above-mentioned deficiencies, increasing efforts have recently been devoted to the collection of high-resolution ( $\geq 1$  Hz) ground-based irradiance data using networks of multiple (up to 99) synchronized photodiode pyranometers deployed over extended domains (between about 1 km<sup>2</sup> and 80 km<sup>2</sup>), some of which are readily available online [59–63].

Altogether, there is a large body of literature touching on various aspects of irradiance variability and its underlying processes in time and space. Recent topics of interest – especially in the realm of small scales – have included, for example,

- the analysis of power spectra and non-linear characteristics of PV power and solar irradiance time series [16,17,32,35,42,43,48,64–68],
- the comparison of power fluctuations from specific PV plants with corresponding irradiance measurements [25,43,57,69],
- the characterization of power variability as a function of PV plant size [13,25,36,44],
- the assessment of the effects of partial shadowing on performance reduction from single modules to entire PV systems [51,70–72],
- the development of methods to infer irradiance and PV power estimates from whole sky images [47,73–81],
- the proposition of classification schemes and measures to quantify variability [25,38,39,82–87],
- the estimation of spatial smoothing, including correlation structures and decorrelation length scales of irradiance and PV power, as well as their increments [10–12,15,26,29,33,37,39,40,49,55,57,58,88–93], and
- the consideration of temporal averaging effects and differences in temporal variability on time scales ranging from seconds to hours, including statistical downscaling [9,54,86,94–104].

With an emphasis on the three last-mentioned research topics and on sub-minute scales below about 10 km, this short review article summarizes previous findings from the literature and concisely recapitulates the essentials of characterizing normalized time-scale-specific changes in irradiance (Sec. 2), as well as quantifying variability (Sec. 3) and averaging effects in space (Sec. 4) and time (Sec. 5). The paper complements previous textbooks and literature reviews on solar energy forecasting and resource assessment [105,106], the estimation of variability in different renewable resources [14,107], and small-scale structures of irradiance fields [108].

## 2. Irradiance normalization and time-scale-specific changes

It is well known that variability in global horizontal irradiance (GHI) can generally be influenced by both astronomical and atmospheric processes [105]. On the one hand, the former give rise to diurnal and seasonal variations, which are accurately predictable and not large on short sub-minute time scales. On the other hand, weather-related phenomena constitute a complex set of influences on GHI over a broad range of time scales (e.g., cloud dynamics can affect the seasonal cycle in GHI as well as its sub-minute variability characteristics). Some studies aim to focus on the actual magnitude of irradiance including all afore-mentioned influences, but occasionally employ a normalization to irradiance under standard test conditions (STC)  $G_{STC} = 1000 \text{ Wm}^{-2}$  [25,38]. In order to study the stochastic nature of weather-induced variability on short time scales, most authors take measures to

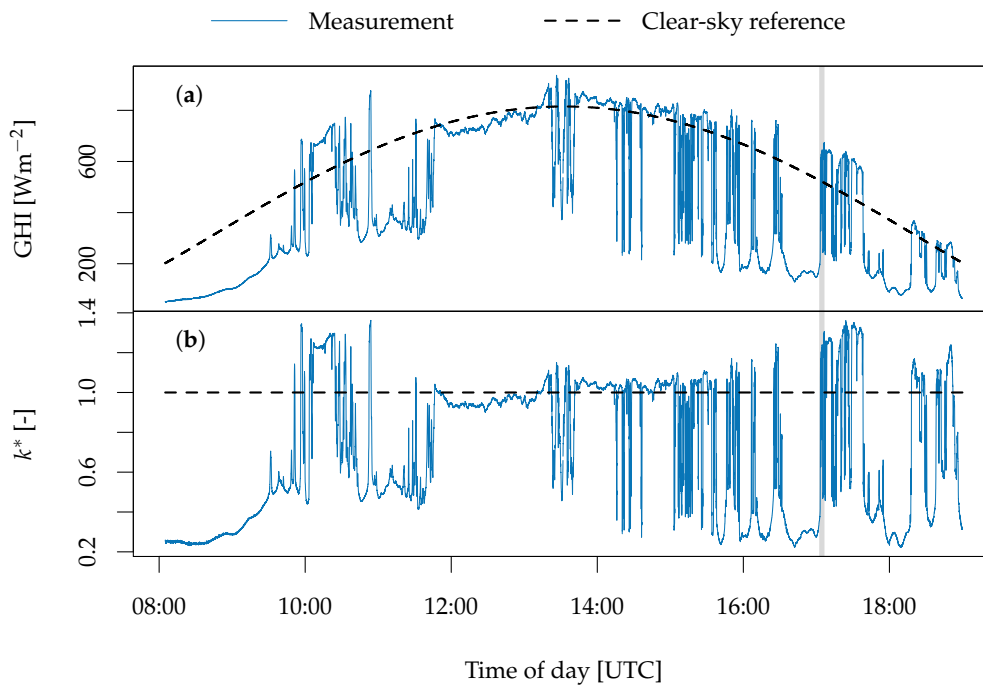


**Figure 1.** (a) An example of a diurnal cycle of measured global horizontal irradiance (GHI) along with simulated clear-sky irradiance derived by a basic model [113]. (b) A corresponding clear-sky index estimate  $k^*$  according to Eq. (2). The data were measured with 1 Hz temporal resolution near Jülich, Germany, on April 25, 2013 and have been conditioned to exclude times of low solar elevation angles  $\alpha < 15^\circ$  after sunrise and before sunset.

remove deterministic trends from GHI time series  $G$  by estimating either the clearness index (a.k.a. transmission coefficient [e.g., 19])

$$k = \frac{G}{G_{extra}} \quad (1)$$

or the clear-sky index

$$k^* = \frac{G}{G_{clear}}. \quad (2)$$

The clearness index represents a normalization of  $G$  to the extraterrestrial solar radiation  $G_{extra}$  (i.e., irradiance at a particular location if there were no atmosphere), while the clear-sky index relates  $G$  to a theoretical clear-sky radiation  $G_{clear}$  (i.e., irradiance at a particular location with a cloud-free atmosphere). The extraterrestrial solar radiation  $G_{extra}$  depends only on astronomical relationships, whereas the characteristics of  $G_{clear}$  depend on parameters of atmospheric conditions and are thus model specific. Many different clear-sky models have been proposed to date [109–112] and the use of any of them introduces unique uncertainties to the  $k^*$  time series, which are absent from the original GHI measurements. With  $G_{clear}$  thus not being unambiguously defined, its values represent typical rather than effective clear-sky irradiance. Nevertheless, many authors have favored the clear-sky index over the clearness index, although nomenclature varies and some call  $k^*$  as defined in Eq. (2) “clearness index” [e.g., 86].

Figure 1 presents a 1 Hz example time series of global horizontal irradiance measured during the HOPE campaign [114], simulated clear-sky irradiance derived by a basic model [113], and estimated clear-sky index as per Eq. (2) in panels (a) and (b). Several typical features of the clear-sky index

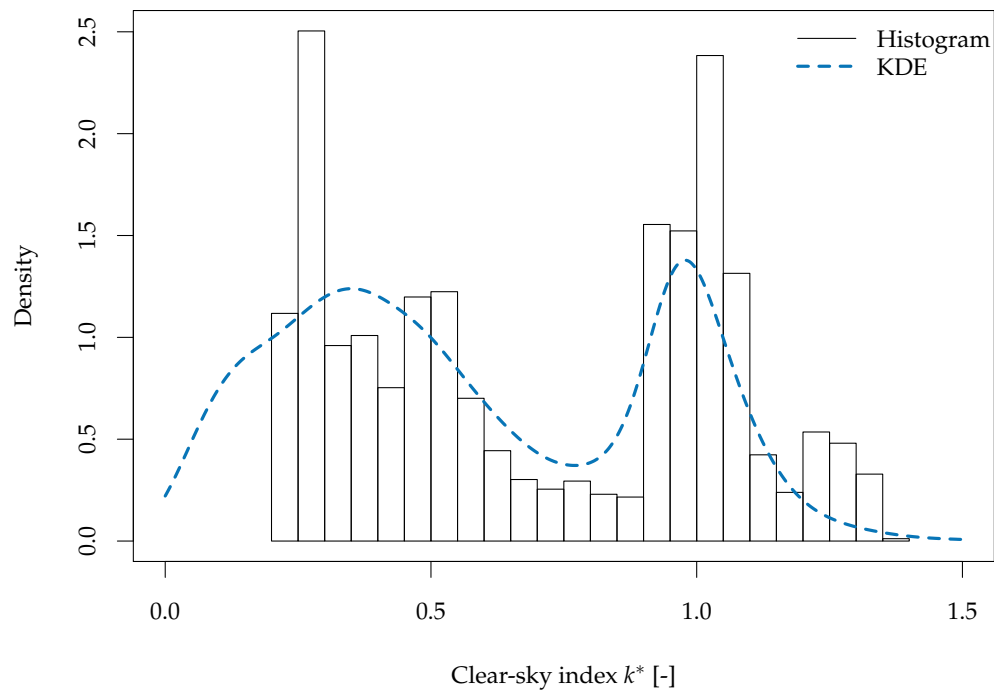


**Figure 2.** Probability density estimates of clear-sky index  $k^*$  based on the single-day example time series previously shown in Fig. 1 (histogram, black lines), as well as a considerably longer series containing a total of about  $4.5 \cdot 10^6$  s worth of single-sensor 1 Hz measurements (kernel density estimate, KDE, dashed blue line). The KDE was derived using Gaussian kernels with a smoothing bandwidth (i.e., smoothing kernel standard deviation) of 0.05.

are evident in the time series. For example, the lowest clear-sky index values are typically not zero, because even the darkest of clouds do not attenuate all irradiance. Additionally, the upper limit can exceed 1, primarily due to short-term reflections from the sides of clouds (and also to a secondary degree due to the limitations of clear-sky models). This phenomenon, known as cloud enhancement, can cause single-point GHI to exceed its corresponding clear-sky irradiance value by more than 50% on sub-minute time scales under broken cloud conditions [16,52,53,115–118]. However, cloud enhancement cannot be unambiguously identified using absolute values of  $k^*$ , because these can be biased by the clear-sky model of choice.

On these short time scales, the probability density function of clear-sky index time series is typically bimodal in nature, with the two peaks respectively corresponding to cloud-covered and cloud-free states [21–23,119,120]. Figure 2 correspondingly shows two estimates of the clear-sky index probability density function based on a histogram of the example time series shown in panel (b) of Fig. 1, as well as a kernel density estimate (KDE) [121] of all available data from that sensor (about  $4.5 \cdot 10^6$  s worth of 1 Hz data). While the histogram does not represent a perfectly bi-modal distribution due to the limited number of data available from the single-day example, the kernel density estimate clearly illustrates the two peaks corresponding to times of overcast and clear skies.

The statistical moments associated with a given clear-sky index time series of length  $T$ , such as the sample arithmetic mean

$$\bar{k}^* = \frac{1}{T} \sum_{t=1}^T k^*(t), \quad (3)$$

and the sample standard deviation

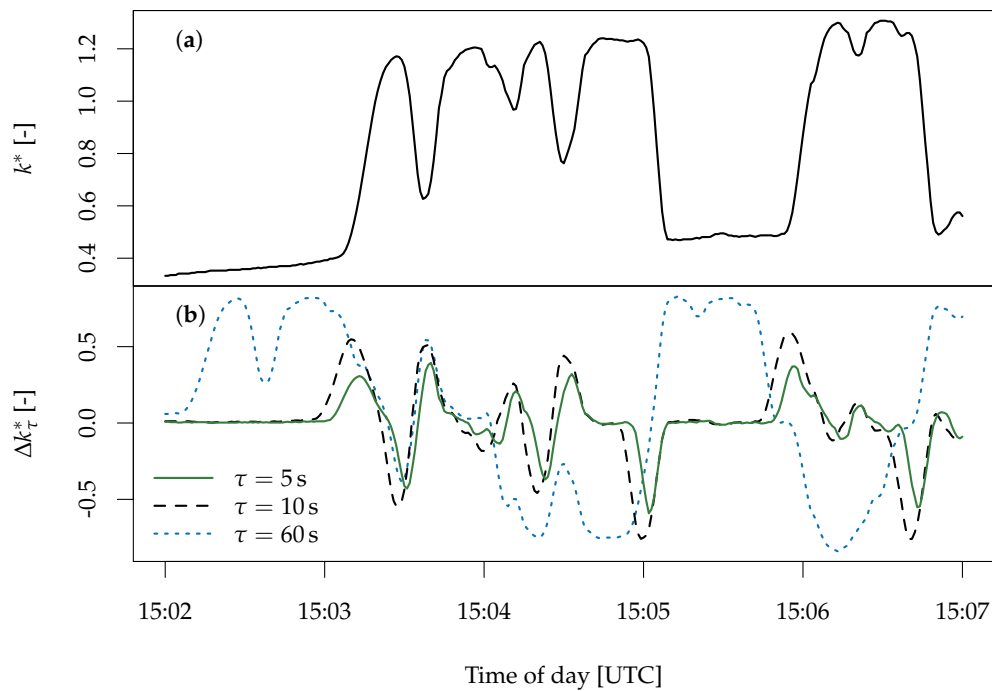


**Figure 3.** A five-minute subset of the time series previously shown in Fig. 1 (there indicated by a vertical gray line); (a) Clear-sky index  $k^*$  time series; (b) Corresponding clear-sky index increments  $\Delta k_\tau^*(t)$  as per Eq. (5) for three distinct short-term increment time steps  $\tau = 5$  s,  $\tau = 10$  s, and  $\tau = 60$  s.

$$\sigma^{k^*} = \sqrt{\frac{1}{T-1} \sum_{t=1}^T (k^*(t) - \bar{k}^*)^2} \quad (4)$$

can be used to characterize the time series's variability to a degree [39]. However, these measures are independent of the observations' ordering in time and, thus, do not quantify how quickly the values of  $k^*$  can change (i.e., randomly shuffling all clear-sky index data in time will affect neither the respective probability density function nor the corresponding moments). Instead, characterizations of clear-sky index variability can be geared towards changes over specified intervals of time  $\tau$  by deriving statistics of  $k^*$  increments

$$\Delta k_\tau^*(t) = k^*(t + \tau) - k^*(t), \quad (5)$$

which are a useful measure of intermittency [122]. Figure 3 presents an illustrative example of thusly derived clear-sky index increments for three distinct short-term increment time steps  $\tau = 5$  s,  $\tau = 10$  s, and  $\tau = 60$  s, based on a five-minute subset of the data previously shown in Fig. 1. The short duration of the series was specifically selected to facilitate an intuitive comprehension of the nature of increment time series.

The probability density functions of single-point clear-sky index increments generally exhibit a narrow central peak (corresponding to a high probability of relatively small increments), surrounded by broad tails in which the probabilities slowly decrease. For increasing increment time steps, the numbers of high-magnitude changes increase as well, leading to more pronounced tails of the corresponding distributions [65]. These general characteristics are illustrated for the same three time steps as before ( $\tau = 5$  s,  $\tau = 10$  s, and  $\tau = 60$  s) by means of kernel density estimates in Fig. 4, using the same data as for the KDE in Fig. 2, i.e., about  $4.5 \cdot 10^6$  s worth of 1 Hz clear-sky index data.

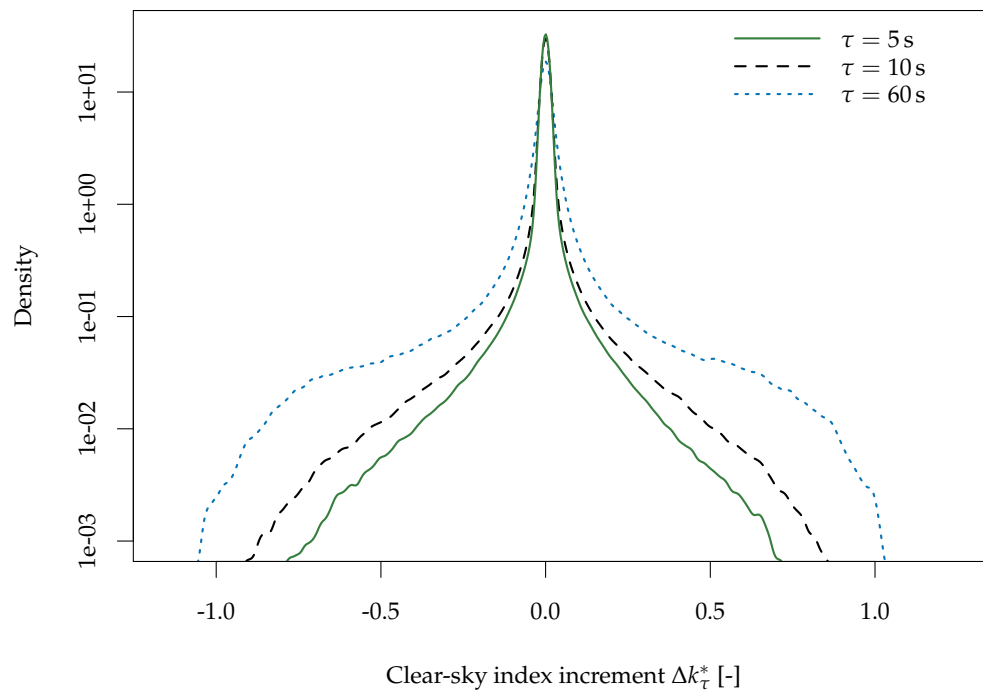


**Figure 4.** Kernel density estimates of clear-sky index increments, based on about  $4.5 \cdot 10^6$  s worth of single-sensor 1 Hz data. The estimates were derived for increment time steps  $\tau = 5$  s,  $\tau = 10$  s, and  $\tau = 60$  s using Gaussian kernels with smoothing bandwidth of 0.01.

Comparisons of spatially averaged increment distributions of multiple pyranometers (or PV plants of different capacities) indicate that the numbers of high-magnitude changes and, thus, the width of the increment distribution are reduced for an increasing number of sensors (or larger PV plants) [25,36,44]. However, the presence of higher-than-normal (i.e., compared to a Gaussian distribution) probabilities of relatively high-magnitude increments remains typical on all scales, with changes of up to tens of standard deviations away from the mean being recorded on a regular basis [32,90]. Similarly, temporal averaging on scales  $\gtrsim 1$  s can also result in a narrowing of increment distributions, and hence a potential underestimation of actual variability [97]. Yet, this drawback can be acceptable, for example, when variability at different locations is compared by means of data featuring diverse temporal resolutions [38].

### 3. Variability quantification

Several different single-number metrics have been proposed to quantify variability in irradiance, normalized irradiance, and/or PV power (some of the underlying concepts can be applied to several of these quantities) within a well-defined period. These include specialized measures, such as the variability index (VI) [82], which is tailored specifically to employ measured irradiance  $G$  and simulated clear-sky irradiance  $G_{clear}$ , and is defined as

$$VI = \frac{\sum_{t=1}^{T-1} \sqrt{[G(t+1) - G(t)]^2 + \Delta T^2}}{\sum_{t=1}^{T-1} \sqrt{[G_{clear}(t+1) - G_{clear}(t)]^2 + \Delta T^2}} \quad (6)$$

with  $T$  denoting the number of consecutive observations and  $\Delta T$  representing the averaging interval of the time series (e.g.,  $\Delta T = 1$  for minute-averaged irradiance measurements). In contrast, the

intra-hour variability score (IHVS) [84] and the daily aggregate ramp rate (DARR) [25] have also been proposed to be used with irradiance data, but can easily be adapted to other quantities, because they simply represent the sum of all absolute increment values during a given hour, or day, respectively. For example, the DARR of any time series  $X$  can be defined as

$$\text{DARR} = \sum_{t=1}^{T-1} \frac{|X(t+1) - X(t)|}{C} \quad (7)$$

with  $T$  again denoting the number of consecutive observations and  $C$  representing an (optional) scaling constant (e.g., for irradiance,  $C = 1000 \text{ Wm}^{-2}$  can be used to normalize to STC [25]). The variability score (VS) [38] is another versatile measure, which can be defined for any time step  $\tau$  as

$$\text{VS}_\tau = \max[\Delta X_0 \times P(|\Delta X_\tau| > \Delta X_0)] \quad (8)$$

with  $\Delta X_\tau = X(t + \tau) - X(t)$  denoting all increments of  $X$  using time step  $\tau$  (i.e., analogous to Eq. (5)),  $\Delta X_0$  consisting of values between 0 and  $\max(|\Delta X_\tau|)$ , and  $P(|\Delta X_\tau| > \Delta X_0)$  representing the probability of absolute increment values greater than  $\Delta X_0$  to occur. In its original formulation, the VS is calculated based on increments in temporally averaged data, with averaging time scale  $\Delta T = \tau$ , and it is expressed as a percentage, with  $\Delta X_\tau$  and  $\Delta X_0$  representing either increments in irradiance normalized to STC or increments in rated PV power capacity [38]. However, the concept of the variability score can generally also be applied to other time series, such as clearness index or clear-sky index. The variability score compares well to the variability index, as both yield comparable estimations of variability with a very high linear correlation between the two measures for a given time scale [15,38].

Finally, changes in the variability of any increment time series  $\Delta X_\tau$  are also reflected by changes of the corresponding standard deviation

$$\sigma^{\Delta X_\tau} = \sqrt{\frac{1}{T-1} \sum_{t=1}^T [\Delta X_\tau(t) - \overline{\Delta X_\tau}]^2} \quad (9)$$

with  $T$  denoting the number of increment values in the series, and  $\overline{\Delta X_\tau}$  representing the mean increment values (in practice,  $\overline{\Delta X_\tau} \rightarrow 0$ ). Increment standard deviation  $\sigma^{\Delta X_\tau}$  characterizes typical excursions from the mean and has become a well-established measure to quantify variability in irradiance, clear-sky index, and PV power output [10,14,18,27,39,97]. For example, when considering averaged  $k^*$  time series across multiple pyranometers, the standard deviation is particularly convenient as it will change as  $n^{-0.5}$  for a number of  $n$  uncorrelated locations, irrespective of the underlying distribution of the data. Note, however, that the non-Gaussian character of irradiance-related increment statistics causes the standard deviation to not necessarily represent the size of extreme fluctuations appropriately. For example, the universal three-sigma rule of thumb, according to which a range of  $\pm 3\sigma^{\Delta X_\tau}$  around the mean would cover 99.73% of the values if  $\Delta X_\tau$  were normally distributed [123], can be misleading when applied to fluctuations in irradiance, clear-sky index, or PV power.

Figure 5 compares daily values of the clear-sky index variability score  $\text{VS}_\tau^{k^*}$  (cf. Eq. (8)) and the clear-sky index increment standard deviation  $\sigma^{\Delta k^*}$  (cf. Eq. (9)) for three distinct time steps  $\tau = 5 \text{ s}$ ,  $\tau = 10 \text{ s}$ , and  $\tau = 60 \text{ s}$ . Although increasing standard deviations generally correspond to increasing variability scores, there is considerable spread around the least-square fits shown in Fig. 5. Consequentially, the coefficients of determination  $0.60 \lesssim R^2 \lesssim 0.65$  associated with the fits only indicate a moderate correlation between the two quantities considered. As both measures are actively being used to quantify variability throughout the literature, it may be worth while to systematically compare the two in a more detailed manner in order to improve the interpretability of their values. However, such an analysis would go beyond the scope of this review.

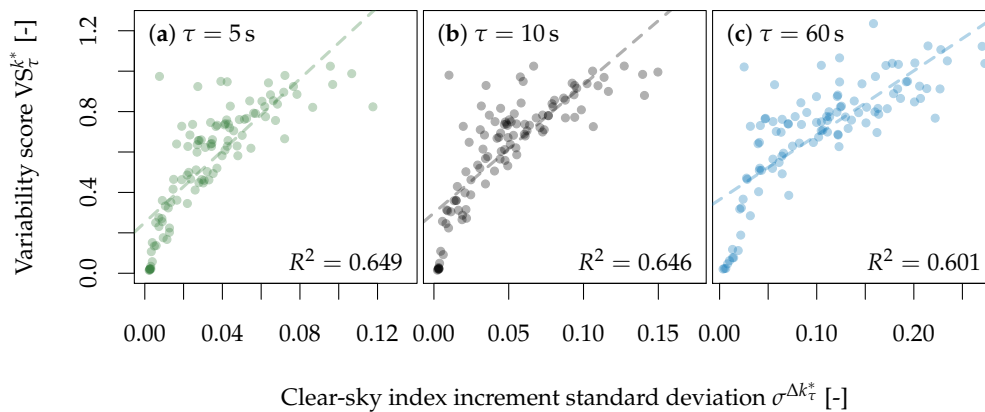


**Figure 5.** A comparison between daily values of the clear-sky index variability score  $VS_{\tau}^{k*}$  (cf. Eq. (8)) and the clear-sky index increment standard deviation  $\sigma^{\Delta k_{\tau}^{k*}}$  (cf. Eq. (9)) for three distinct time steps (a)  $\tau = 5$  s, (b)  $\tau = 10$  s, and (c)  $\tau = 60$  s, using 105 days worth of single-sensor 1 Hz clear-sky index estimates (i.e., the same data as in Fig. 4). Least-square fits are included as dashed lines and the corresponding coefficients of determination  $R^2$  are quoted in each panel.

Additionally, a number of studies have applied classification schemes in order to group sets of time series according to their variability characteristics. Typically, the resulting variability classes are made up of at least “high-variability”, “medium-variability”, and “low-variability” [83], although the nomenclature varies (e.g., high variability can be called “mixed-sky”, medium variability “clear-sky”, and low variability “overcast” [39]). Some authors split the range of a single-number metric into subsets using fixed thresholds [87], while others employ multivariate classification schemes [39,86] or machine learning algorithms [83,85].

#### 4. Spatial averaging

In general, the larger the panel-covered area of a PV system, the less variable its power output is compared to a single-point irradiance measurement [25], especially on short sub-minute time scales [43,44]. Similarly, spatial smoothing causes substantial differences between the variability characteristics of single utility-scale PV plants covering relatively small areas, and a large number of distributed systems with similar total capacities, but spanning relatively large areas [27]. In lieu of suitable PV power data, averages of irradiance or clear-sky index increments can provide an estimate of the output variability of an ensemble of PV installations at multiple locations [10].

An illustrative example of spatial averaging is shown in Fig. 6, where single-sensor clear-sky index estimates are contrasted with the spatially averaged values of up to 99 synchronized pyranometers dispersed over an area of approximately 80 km<sup>2</sup> in panel (a), and 1 min increments are shown for both the single sensor and the spatial average in panel (b). Pronounced spatial smoothing is evident in both panels.

As a characterization of the spatial structure of  $\Delta k_{\tau}^{k*}$  fields, it is useful to consider spatial two-point correlation coefficients between locations  $i$  and  $j$

$$\rho_{ij}^{\Delta k_{\tau}^{k*}} = \frac{\sum_{t=1}^T (\Delta k_{\tau,i}^{k*}(t) - \overline{\Delta k_{\tau,i}^{k*}})(\Delta k_{\tau,j}^{k*}(t) - \overline{\Delta k_{\tau,j}^{k*}})}{\sqrt{\sum_{t=1}^T (\Delta k_{\tau,i}^{k*}(t) - \overline{\Delta k_{\tau,i}^{k*}})^2 \sum_{t=1}^T (\Delta k_{\tau,j}^{k*}(t) - \overline{\Delta k_{\tau,j}^{k*}})^2}}, \quad (10)$$

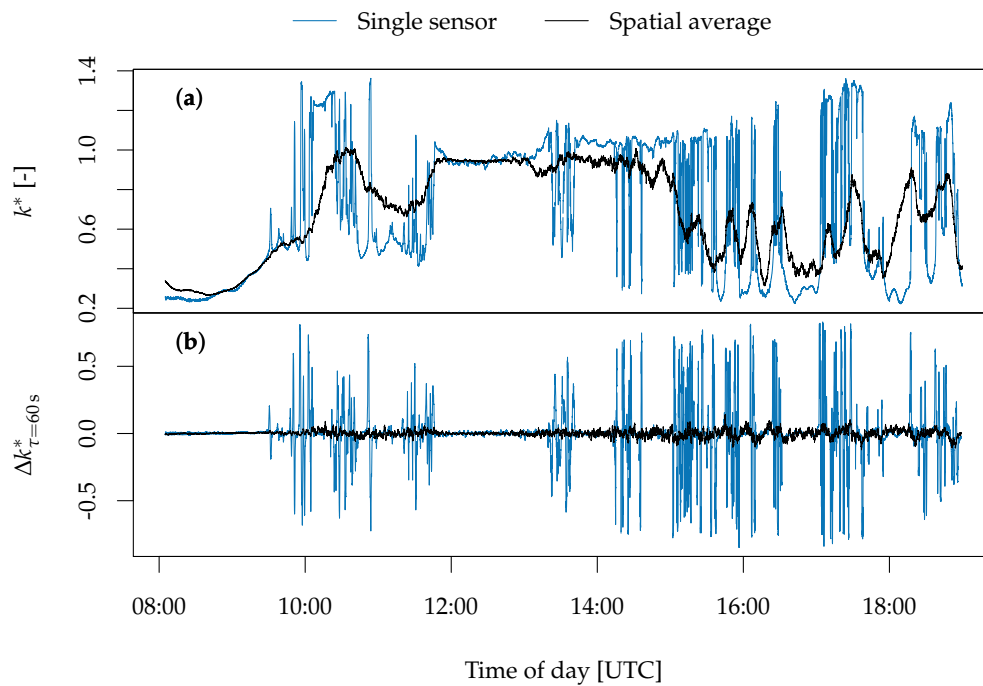


**Figure 6.** An example of spatial averaging: (a) the same 1 s single-sensor clear-sky index  $k^*$  time series as in Fig. 1 along with a corresponding spatially averaged 1 s clear-sky index computed over as many as 99 pyranometers dispersed over an area of about 80 km<sup>2</sup>; (b) 1 min clear-sky index increments  $\Delta k^*_{\tau}$  derived according to Eq. (5) for both the single-sensor time series and the spatial average.

which govern the process of spatial averaging (i.e., the standard deviation  $\sigma_{x+y}$  of the sum of two random variables  $x + y$  with correlation coefficient  $\rho_{xy}$  is  $\sigma_{x+y} = \sqrt{\sigma_x^2 + \sigma_y^2 + 2\rho_{xy}\sigma_x\sigma_y}$ ). In Eq. (10),  $\Delta k^*_{\tau,i}(t)$  and  $\Delta k^*_{\tau,j}(t)$  are the two individual increment time series at the two locations  $i$  and  $j$ , while  $\overline{\Delta k^*_{\tau,i}}$  and  $\overline{\Delta k^*_{\tau,j}}$  are the corresponding arithmetic means (computed as in Eq. (3)), and the quantity  $T$  denotes the number of data points in each of the two time series.

These correlation structures can be used, for example, to directly predict power variability of large and/or distributed PV systems based on a single pyranometer, using a wavelet approach [36,46,69,83]. Increment correlations (both in space and time) have been shown to depend on effective cloud speed [10,27], different daily variability categories [12,83], and short-term sky types [39]. Moreover, correlation coefficients can depend on the orientation of a sensor pair relative to the direction of cloud movement [37,40,55,58,89]. For all quantities and methods considered, increment correlations at different locations have been shown to decrease with increasing distance, with a smaller rate of decrease (longer decorrelation distances) for larger time increments. For along-wind correlations, the presence of negative peaks in the increment correlation structures has been suggested [11,12,37,57,58].

Several models have been proposed to predict the behavior of increment correlation as a function of distance for specific temporal scales by using empirical fits to measured data [10,12,57,83,89,90,92] and/or by modeling simplified cloud shapes as randomly positioned and subsequently blurred squares [57], unions of randomly positioned discs [55], double-sigmoidal clear-sky index deviations [58], or fractal structures [40]. For example, hourly satellite-derived irradiance data from three different locations in the United States were used to analyze two-point correlations of  $k^*$  increments as a function of pair distance, with samples being separated in the range of  $10 \text{ km} \leq d_{ij} \leq 300 \text{ km}$  [10]. Taking increment time lags of  $1 \text{ h} \leq \tau \leq 4 \text{ h}$  and estimated relative cloud speed  $v$  into account, the correlation structure was estimated as  $\rho_{ij}^{\Delta k^*_{\tau}} = (1 + d_{ij} \cdot \tau^{-1} \cdot v^{-1})^{-1}$ , implying a linear relationship between

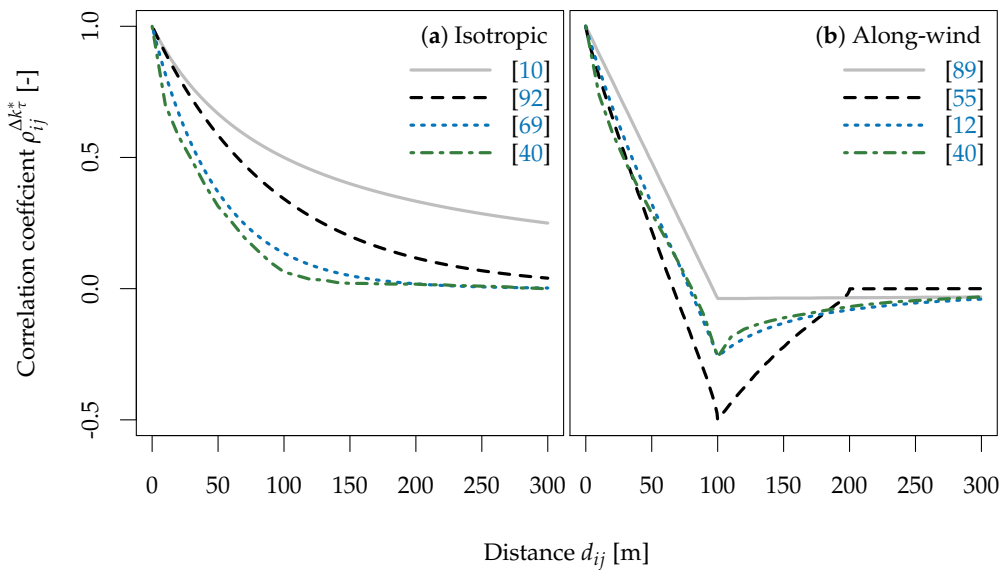


**Figure 7.** Some examples of previously proposed models to estimate the two-point correlation coefficient of clear-sky index increments  $\rho_{ij}^{\Delta k_{\tau}^*}$  as a function of distance  $d_{ij}$  for increment time scale  $\tau = 10$  s and cloud speed  $v = 10 \text{ ms}^{-1}$ . Panel (a) shows examples of isotropic (i.e., without considering the direction of cloud motion) correlation structures proposed by Hoff and Perez [10], Perez *et al.* [92], and Lave *et al.* [69] (each derived from simple equations implying a linear relationship between  $d_{ij}$ ,  $\tau$  and  $v$ ), as well as Lohmann *et al.* [40] (based on 3 h worth of 1 Hz  $k^*$  field data simulated by a fractal cloud model with an assumed average cloud cover of 50%). Panel (b) presents along-wind structures according to models proposed by Lonij *et al.* [89], Arias-Castro *et al.* [55], and Widén [12] (the presented curves were extracted from Elsinga and van Sark [58]; cf. their Fig. 2), as well as the afore-mentioned fractal model [40].

pair distance  $d_{ij}$  and time lag  $\tau$  for fixed values of the correlation coefficient. Similar implications were made by other proposed models, for example  $\rho_{ij}^{\Delta k_{\tau}^*} = \exp(d_{ij} \cdot \ln(0.2) \cdot 1.5^{-1} \cdot \tau^{-1} \cdot v^{-1})$  [92] and  $\rho_{ij}^{\Delta k_{\tau}^*} = \exp(-\frac{d_{ij}}{0.5 \cdot \tau \cdot v})$  [57,69]. These models were obtained as curve fits from different data with relatively coarse spatiotemporal resolutions.

Figure 7 contrasts estimated two-point correlation coefficients of clear-sky index increments  $\rho_{ij}^{\Delta k_{\tau}^*}$  as a function of distance  $d_{ij}$  for increment time scale  $\tau = 10$  s and cloud speed  $v = 10 \text{ ms}^{-1}$ , based on several proposed models [10,12,40,55,69,89,92]. Isotropic structures obtained without regards to the direction of cloud motion as well as structures calculated along the main wind direction are respectively considered in panels (a) and (b). While each isotropic curve in panel (a) decreases monotonously from 1 towards 0 for increasing distances, the rate of decrease differs considerably between models. For example, at a pair distance of  $d_{ij} \approx 100$  m model results range between  $0 \lesssim \rho_{ij}^{\Delta k_{\tau}^*} \lesssim 0.5$ . Similarly, all along-wind correlation structures in panel (b) decrease with distinct rates for increasing distances up to  $d_{ij} = 100$  m, where differences between models range between  $-0.5 \lesssim \rho_{ij}^{\Delta k_{\tau}^*} \lesssim 0$ . For further increasing distances  $d_{ij} > 100$  m, each curve transitions to its own unique character of constant or increasing correlation coefficients, approaching 0.

## 5. Temporal averaging

Similar to spatial averaging, irradiance variability is reduced when considering temporally averaged data. Figure 8 presents examples of such temporal averaging, based on the example period employed in the previous figures, using two different averaging periods of 1 min and 10 min. Panel (a)

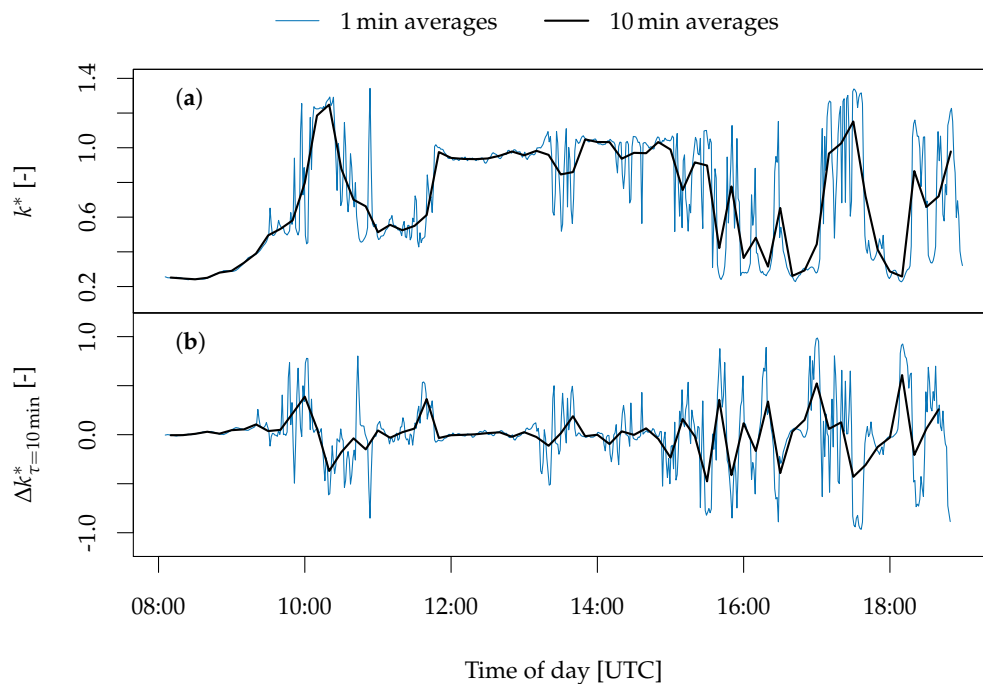


**Figure 8.** An example of temporal averaging: **(a)** Averages of 1 min and 10 min temporal resolutions based on the 1 s single-sensor clear-sky index  $k^*$  time series shown in Fig. 1; **(b)** Corresponding 10 min clear-sky index increments  $\Delta k^*_{\tau}$  derived according to Eq. (5).

shows the clear-sky index time series for these averages, while panel (b) illustrates the averaging effect on 10 min increments in the clear-sky index. The misrepresentation of variability is evident for the longer averaging time in both panels.

As indicated in Sec. 1, ground-based solar irradiance observations have often been averaged using a range of different temporal resolutions (from hours to fractions of a second) and there is no consensus as to the proper resolution needed to capture all relevant variability. Early studies showed temporal averaging on time scales larger than minutes to introduce considerable smoothing to the clear-sky index, and to affect its probability distribution [22,23]. More recent analyses have concluded that the temporal resolution needed to capture irradiance variability on all time scales may be as small as 0.1 s [16,51,53], 0.4 s [15], or 1 s [97]. Those studies which determined the need for second-or-higher resolutions were based on

1. using the 2nd temporal derivative of irradiance as a measure for instantaneous variation, and defining the daily minimum (i.e., negative) value of this derivative as each day's strongest instantaneous irradiance variation, and finally calculating a hypothetical optimal averaging time based on an acceptable error of  $10 \text{ Wm}^{-2}$  and an assumed parabolic shape of the variation for each of a few hundred days in spring and summer [16];
2. analyzing the sample standard deviation of irradiance as a function of averaging time measured during 7 hours on a single summer's day [51];
3. separately studying the variability index and the variability score of irradiance as functions of averaging time for 7 selected days [15]; and
4. characterizing the changes of  $k^*$  and  $\Delta k^*_{\tau}$  standard deviations as a function of averaging time using thousands of hours worth of irradiance measurements with original temporal resolutions between 0.01 and 1 s [97].

In addition to these differences in methods and number of data, some of the studies were limited to specific geographic areas (i.e., Southern Norway [16], Southern Finland [51], and Eastern Canada [15]), while another compared data from four different regions in the Northern Hemisphere (i.e., Eastern Canada, Germany, Hawaii, and Arizona) [97].

In practice, the effectively necessary temporal resolution of data strongly depends on the spatial scale considered. On the one hand, fluctuations of up to  $\pm 50\%$  from one second to the next (and changes of more than 90% within 20 s) have been documented in the feed-in of a relatively small 48 kWp PV plant [44]. On the other hand, considerably larger multi-megawatt utility-scale PV plants may not require high temporal resolutions on the order of seconds for monitoring purposes [124], while minute-averaged data may be too coarsely resolved [25].

In view of the relatively small number of high-resolution datasets available to date, several methods have been proposed to downscale more easily-accessible low-resolution data to smaller scales. For example, Markov-model-based approaches have been applied to 15-min PV power [104], hourly irradiance [98], hourly weather observations [56,95], or daily clearness index [125], in order to simulate variability on temporal scales well below those of the input data. Other downscaling approaches include providing a library of representative high-resolution irradiance samples [126] as well as simulating changes in the clear-sky index differently for different classes of variability [86,103]. A number of other sophisticated methods have been proposed to simulate relatively high-resolution data in time and/or space (using, for example, copulas or Markov chains), but without conditioning to large-scale information [26,29,49,91,127,128]. While these last-mentioned approaches have not been immediately designed to downscale coarsely resolved real-world measurements, they can likely be adapted for this purpose.

## 6. Conclusions

This article concisely reviews recently published essentials from the literature regarding the quantification and small-scale averaging of irradiance variability in time and space. Complementing previous textbooks and literature reviews [14,105–108], the paper emphasizes relatively small sub-minute scales below about 10 km. Despite the many articles touching on the subject of irradiance variability, suitable high-resolution measurement data are still relatively scarce. While some small-scale irradiance data have been publicly released [e.g., 59–63], there is still a need for more high-resolution measurements to robustly validate previous findings [40]. Granting open access to such data and corresponding models is considered best practice in order to foster scientific discussion and facilitate knowledge-based energy policies [129].

With regards to said policies and the applicability of irradiance variability research to PV power systems, there is a need for considering variability in irradiance on tilted surfaces as well as its effects on the processes of energy conversion. While most of the research presented in this review has been based on global horizontal irradiance, PV systems typically feature tilted modules. On a daily basis, irradiance variability on an inclined plane has been shown to be higher than on the horizontal [6,130], but corresponding analyses of high-resolution sub-minute data are still lacking. Likewise, an extensive validation of models separating direct and diffuse irradiance (a necessary step to predict irradiance on an inclined plane as a function of GHI) is not yet possible on sub-minute scales for lack of suitable data (it has, however, recently been performed using minute data [131]). In general, small-scale specific phenomena, such as cloud enhancement, may call for future adaptations and extensions of well-established large-scale-based methods and conclusions [132].

**Acknowledgments:** This article is based in part on the preface of the author's doctoral thesis [133]. Co-supervisor Adam H. Monahan of the University of Victoria, BC, Canada, and external reviewer Jan Kleissl of the University of California, San Diego, USA, are gratefully acknowledged for suggesting to go the extra mile and turn the text into this review paper. Most of this article's figures are based on data courtesy of Andreas Macke of the Leibniz Institute for Tropospheric Research (TROPOS), Leipzig, Germany. The data have been collected during the HOPE campaign [114] and are also available online [61]. The open access publication fund at the University of

Oldenburg and the corresponding financial support of the German Research Foundation (DFG) are acknowledged for covering the costs to publish in open access.

**Conflicts of Interest:** The author declares no conflict of interest.

## References

1. Solar Power Europe (SPE). Solar market report & membership directory, 2016.
2. REN21. Renewables 2016 global status report. Technical report, REN21 Secretariat, Paris, 2016.
3. Haegel, N.M.; Margolis, R.; Buonassisi, T.; Feldman, D.; Froitzheim, A.; Garabedian, R.; Green, M.; Glunz, S.; Henning, H.M.; Holder, B.; Kaizuka, I.; Kroposki, B.; Matsubara, K.; Niki, S.; Sakurai, K.; Schindler, R.A.; Tumas, W.; Weber, E.R.; Wilson, G.; Woodhouse, M.; Kurtz, S. Terawatt-scale photovoltaics: Trajectories and challenges. *Science* **2017**, *356*, 141. doi:10.1126/science.aal1288.
4. Stetz, T.; von Appen, J.; Niedermeyer, F.; Scheibner, G.; Sikora, R.; Braun, M. Twilight of the grids: The impact of distributed solar on Germany's energy transition. *Power and Energy Magazine, IEEE* **2015**, *13*, 50–61. doi:10.1109/MPE.2014.2379971.
5. Perez, R.; Rábago, K.R.; Trahan, M.; Rawlings, L.; Norris, B.; Hoff, T.; Putnam, M.; Perez, M. Achieving very high PV penetration – The need for an effective electricity remuneration framework and a central role for grid operators. *Energy Policy* **2016**, *96*, 27–35. doi:10.1016/j.enpol.2016.05.016.
6. Suri, M.; Huld, T.; Dunlop, E.; Albuissou, M.; Lefevre, M.; Wald, L. Uncertainties in solar electricity yield prediction from fluctuation of solar radiation. 22nd European Photovoltaic Solar Energy Conference, 2007.
7. Bridier, L.; David, M.; Lauret, P. Optimal design of a storage system coupled with intermittent renewables. *Renewable Energy* **2014**, *67*, 2–9. doi:10.1016/j.renene.2013.11.048.
8. Denholm, P.; Hand, M. Grid flexibility and storage required to achieve very high penetration of variable renewable electricity. *Energy Policy* **2011**, *39*, 1817–1830.
9. Widén, J.; Wäckelgård, E.; Paatero, J.; Lund, P. Impacts of distributed photovoltaics on network voltages: Stochastic simulations of three Swedish low-voltage distribution grids. *Electric Power Systems Research* **2010**, *80*, 1562–1571. doi:10.1016/j.epsr.2010.07.007.
10. Hoff, T.E.; Perez, R. Modeling PV fleet output variability. *Solar Energy* **2012**, *86*, 2177–2189. doi:10.1016/j.solener.2011.11.005.
11. Perez, R.; Kivalov, S.; Schlemmer, J.; Hemker Jr, K.; Hoff, T.E. Short-term irradiance variability: Preliminary estimation of station pair correlation as a function of distance. *Solar Energy* **2012**, *86*, 2170–2176.
12. Widén, J. A model of spatially integrated solar irradiance variability based on logarithmic station-pair correlations. *Solar Energy* **2015**, *122*, 1409–1424. doi:10.1016/j.solener.2015.10.043.
13. Lave, M.; Kleissl, J.; Arias-Castro, E. High-frequency irradiance fluctuations and geographic smoothing. *Solar Energy* **2012**, *86*, 2190–2199. doi:10.1016/j.solener.2011.06.031.
14. Widén, J.; Carpmann, N.; Castellucci, V.; Lingfors, D.; Olauson, J.; Remouit, F.; Bergkvist, M.; Grabbe, M.; Waters, R. Variability assessment and forecasting of renewables: A review for solar, wind, wave and tidal resources. *Renewable and Sustainable Energy Reviews* **2015**, *44*, 356–375. doi:10.1016/j.rser.2014.12.019.
15. Gagné, A.; Turcotte, D.; Goswamy, N.; Poissant, Y. High resolution characterisation of solar variability for two sites in Eastern Canada. *Solar Energy* **2016**, *137*, 46–54. doi:10.1016/j.solener.2016.07.042.
16. Yordanov, G.; Saetre, T.; Midtgard, O.M. Optimal temporal resolution for detailed studies of cloud-enhanced sunlight (Overirradiance). *Photovoltaic Specialists Conference (PVSC), 2013 IEEE 39th* **2013**, pp. 0985–0988. doi:10.1109/PVSC.2013.6744306.
17. Klima, K.; Apt, J. Geographic smoothing of solar PV: results from Gujarat. *Environmental Research Letters* **2015**, *10*, 104001. doi:10.1088/1748-9326/10/10/104001.
18. Perez, R.; David, M.; Hoff, T.E.; Jamaly, M.; Kivalov, S.; Kleissl, J.; Lauret, P.; Perez, M. Spatial and temporal variability of solar energy. *Foundations and Trends® in Renewable Energy* **2016**, *1*, 1–44. doi:10.1561/27000000006.
19. Liu, B.Y.; Jordan, R.C. The interrelationship and characteristic distribution of direct, diffuse and total solar radiation. *Solar Energy* **1960**, *4*, 1–19. doi:10.1016/0038-092X(60)90062-1.
20. Bendt, P.; Collares-Pereira, M.; Rabl, A. The frequency distribution of daily insolation values. *Solar Energy* **1981**, *27*, 1–5. doi:10.1016/0038-092X(81)90013-X.

21. Jurado, M.; Caridad, J.; Ruiz, V. Statistical distribution of the clearness index with radiation data integrated over five minute intervals. *Solar Energy* **1995**, *55*, 469–473. doi:10.1016/0038-092X(95)00067-2.
22. Skartveit, A.; Olseth, J. The probability density and autocorrelation of short-term global and beam irradiance. *Solar Energy* **1992**, *49*, 477–487. doi:10.1016/0038-092X(92)90155-4.
23. Suehrcke, H.; McCormick, P.G. The frequency distribution of instantaneous insolation values. *Solar Energy* **1988**, *40*, 413–422.
24. Tomson, T.; Tamm, G. Short-term variability of solar radiation. *Solar Energy* **2006**, *80*, 600–606. doi:10.1016/j.solener.2005.03.009.
25. van Haaren, R.; Morjaria, M.; Fthenakis, V. Empirical assessment of short-term variability from utility-scale solar PV plants. *Progress in Photovoltaics: Research and Applications* **2014**, *22*, 548–559. doi:10.1002/pip.2302.
26. Munkhammar, J.; Widén, J. An autocorrelation-based copula model for generating realistic clear-sky index time-series. *Solar Energy* **2017**, *158*, 9–19. doi:10.1016/j.solener.2017.09.028.
27. Hoff, T.E.; Perez, R. Quantifying PV power output variability. *Solar Energy* **2010**, *84*, 1782–1793.
28. Perez, R.; Kivalov, S.; Schlemmer, J.; Hemker, K.; Hoff, T. Parameterization of site-specific short-term irradiance variability. *Solar Energy* **2011**, *85*, 1343–1353. doi:10.1016/j.solener.2011.03.016.
29. Munkhammar, J.; Widén, J.; Hinkelman, L.M. A copula method for simulating correlated instantaneous solar irradiance in spatial networks. *Solar Energy* **2017**, *143*, 10–21.
30. Woyte, A.; Van Thong, V.; Belmans, R.; Nijs, J. Voltage fluctuations on distribution level introduced by photovoltaic systems. *Energy Conversion, IEEE Transactions on* **2006**, *21*, 202–209. doi:10.1109/TEC.2005.845454.
31. Woyte, A.; Belmans, R.; Nijs, J. Localized spectral analysis of fluctuating power generation from solar energy systems. *EURASIP Journal on Advances in Signal Processing* **2007**, *2007*.
32. Anvari, M.; Lohmann, G.; Wächter, M.; Milan, P.; Lorenz, E.; Heinemann, D.; Tabar, M.R.R.; Peinke, J. Short term fluctuations of wind and solar power systems. *New Journal of Physics* **2016**, *18*, 063027. doi:10.1088/1367-2630/18/6/063027.
33. Barry, J.; Munzke, N.; Thomas, J. Power fluctuations in solar-storage clusters: spatial correlation and battery response times. *Energy Procedia* **2017**, *135*, 379–390. doi:10.1016/j.egypro.2017.09.516.
34. Bosch, J.; Kleissl, J. Cloud motion vectors from a network of ground sensors in a solar power plant. *Solar Energy* **2013**, *95*, 13–20. doi:10.1016/j.solener.2013.05.027.
35. Calif, R.; Schmitt, F.G.; Huang, Y.; Soubdhan, T. Intermittency study of high frequency global solar radiation sequences under a tropical climate. *Solar Energy* **2013**, *98*, 349–365. doi:10.1016/j.solener.2013.09.018.
36. Dyreson, A.R.; Morgan, E.R.; Monger, S.H.; Acker, T.L. Modeling solar irradiance smoothing for large PV power plants using a 45-sensor network and the Wavelet Variability Model. *Solar Energy* **2014**, *110*, 482–495. doi:10.1016/j.solener.2014.09.027.
37. Hinkelman, L.M. Differences between along-wind and cross-wind solar irradiance variability on small spatial scales. *Solar Energy* **2013**, *88*, 192–203. doi:10.1016/j.solener.2012.11.011.
38. Lave, M.; Reno, M.J.; Broderick, R.J. Characterizing local high-frequency solar variability and its impact to distribution studies. *Solar Energy* **2015**, *118*, 327–337. doi:10.1016/j.solener.2015.05.028.
39. Lohmann, G.M.; Monahan, A.H.; Heinemann, D. Local short-term variability in solar irradiance. *Atmospheric Chemistry and Physics* **2016**, *16*, 6365–6379. doi:10.5194/acp-16-6365-2016.
40. Lohmann, G.M.; Hammer, A.; Monahan, A.H.; Schmidt, T.; Heinemann, D. Simulating clear-sky index increment correlations under mixed sky conditions using a fractal cloud model. *Solar Energy* **2017**, *150*, 255–264. doi:10.1016/j.solener.2017.04.048.
41. Lorenzo, A.T.; Holmgren, W.F.; Cronin, A.D. Irradiance monitoring network data and wind motion vectors, 2015.
42. Madhavan, B.L.; Deneke, H.; Witthuhn, J.; Macke, A. Multiresolution analysis of the spatiotemporal variability in global radiation observed by a dense network of 99 pyranometers. *Atmospheric Chemistry and Physics* **2017**, *17*, 3317–3338. doi:10.5194/acp-17-3317-2017.
43. Marcos, J.; Marroyo, L.; Lorenzo, E.; Alvira, D.; Izco, E. From irradiance to output power fluctuations: the PV plant as a low pass filter. *Progress in Photovoltaics: Research and Applications* **2011**, *19*, 505–510. doi:10.1002/pip.1063.

44. Marcos, J.; Marroyo, L.; Lorenzo, E.; Alvira, D.; Izco, E. Power output fluctuations in large scale PV plants: One year observations with one second resolution and a derived analytic model. *Progress in Photovoltaics: Research and Applications* **2011**, *19*, 218–227. doi:10.1002/pip.1016.
45. Monger, S.H.; Morgan, E.R.; Dyreson, A.R.; Acker, T.L. Applying the kriging method to predicting irradiance variability at a potential PV power plant. *Renewable Energy* **2016**, *86*, 602–610. doi:10.1016/j.renene.2015.08.058.
46. Perpiñán, O.; Lorenzo, E. Analysis and synthesis of the variability of irradiance and PV power time series with the wavelet transform. *Solar Energy* **2011**, *85*, 188–197.
47. Schmidt, T.; Kalisch, J.; Lorenz, E.; Heinemann, D. Evaluating the spatio-temporal performance of sky-imager-based solar irradiance analysis and forecasts. *Atmospheric Chemistry and Physics* **2016**, *16*, 3399–3412. doi:10.5194/acp-16-3399-2016.
48. Tabar, M.R.R.; Anvari, M.; Lohmann, G.; Heinemann, D.; Wächter, M.; Milan, P.; Lorenz, E.; Peinke, J. Kolmogorov spectrum of renewable wind and solar power fluctuations. *The European Physical Journal Special Topics* **2014**, *223*, 1–8. doi:10.1140/epjst/e2014-02217-8.
49. Widén, J.; Shepero, M.; Munkhammar, J. On the properties of aggregate clear-sky index distributions and an improved model for spatially correlated instantaneous solar irradiance. *Solar Energy* **2017**, *157*, 566–580. doi:10.1016/j.solener.2017.08.033.
50. Yordanov, G.H.; Saetre, T.O.; Midtgård, O.M. Extreme overirradiance events in Norway: 1.6 suns measured close to 60°N. *Solar Energy* **2015**, *115*, 68–73. doi:10.1016/j.solener.2015.02.020.
51. Torres Lobera, D.; Mäki, A.; Huusari, J.; Lappalainen, K.; Suntio, T.; Valkealahti, S. Operation of TUT solar PV power station research plant under partial shading caused by snow and buildings. *International Journal of Photoenergy* **2013**, *2013*.
52. Yordanov, G.; Midtgård, O.M.; Saetre, T.; Nielsen, H.; Norum, L. Overirradiance (cloud enhancement) events at high latitudes. *Photovoltaics, IEEE Journal of* **2013**, *3*, 271–277. doi:10.1109/JPHOTOV.2012.2213581.
53. Yordanov, G.H.; Saetre, T.O.; Midtgard, O.M. 100-millisecond Resolution for Accurate Overirradiance Measurements. *IEEE Journal of Photovoltaics* **2013**, *3*, 1354–1360. doi:10.1109/JPHOTOV.2013.2264621.
54. Lave, M.; Broderick, R.J.; Reno, M.J. Solar variability zones: Satellite-derived zones that represent high-frequency ground variability. *Solar Energy* **2017**, *151*, 119–128. doi:10.1016/j.solener.2017.05.005.
55. Arias-Castro, E.; Kleissl, J.; Lave, M. A Poisson model for anisotropic solar ramp rate correlations. *Solar Energy* **2014**, *101*, 192–202. doi:10.1016/j.solener.2013.12.028.
56. Bright, J.M.; Babacan, O.; Kleissl, J.; Taylor, P.G.; Crook, R. A synthetic, spatially decorrelating solar irradiance generator and application to a LV grid model with high PV penetration. *Solar Energy* **2017**, *147*, 83–98. doi:10.1016/j.solener.2017.03.018.
57. Lave, M.; Kleissl, J. Cloud speed impact on solar variability scaling – Application to the wavelet variability model. *Solar Energy* **2013**, *91*, 11–21. doi:10.1016/j.solener.2013.01.023.
58. Elsinga, B.; van Sark, W.G. Analytic model for correlations of cloud induced fluctuations of clear-sky index. *Solar Energy* **2017**, *155*, 985–1001. doi:10.1016/j.solener.2017.07.035.
59. Lorenzo, A.T.; Holmgren, W.F.; Cronin, A.D. Irradiance forecasts based on an irradiance monitoring network, cloud motion, and spatial averaging. *Solar Energy* **2015**, *122*, 1158–1169. doi:10.1016/j.solener.2015.10.038.
60. Natural Resources Canada. High-Resolution Solar Radiation Datasets, 2016.
61. Standardized Atmospheric Measurement Data. Shortwave broadband downwelling shortwave radiation (surface), 2017.
62. Sengupta, M.; Andreas, A. Oahu solar measurement grid (1-year archive): 1-second solar irradiance; Oahu, Hawaii (data). Technical report, 2010.
63. Schmidt, T.; Lohmann, G.M. A 10 Hz irradiance dataset from Oldenburg, Germany. Zenodo, 2018. doi:10.5281/zenodo.1216763.
64. Curtright, A.E.; Apt, J. The character of power output from utility-scale photovoltaic systems. *Progress in Photovoltaics: Research and Applications* **2008**, *16*, 241–247. doi:10.1002/pip.786.
65. Lave, M.; Kleissl, J. Solar variability of four sites across the state of Colorado. *Renewable Energy* **2010**, *35*, 2867–2873.
66. Madanchi, A.; Absalan, M.; Lohmann, G.; Anvari, M.; Reza Rahimi Tabar, M. Strong short-term non-linearity of solar irradiance fluctuations. *Solar Energy* **2017**, *144*, 1–9. doi:10.1016/j.solener.2017.01.008.

67. Anvari, M.; Werther, B.; Lohmann, G.; Wächter, M.; Peinke, J.; Beck, H.P. Suppressing power output fluctuations of photovoltaic power plants. *Solar Energy* **2017**, *157*, 735–743. doi:10.1016/j.solener.2017.08.038.
68. Schmietendorf, K.; Peinke, J.; Kamps, O. The impact of turbulent renewable energy production on power grid stability and quality. *The European Physical Journal B* **2017**, *90*. doi:10.1140/epjb/e2017-80352-8.
69. Lave, M.; Kleissl, J.; Stein, J.S. A wavelet-based variability model (WVM) for solar PV power plants. *IEEE Transactions on Sustainable Energy* **2013**, *4*, 501–509. doi:10.1109/TSTE.2012.2205716.
70. Woyte, A.; Nijs, J.; Belmans, R. Partial shadowing of photovoltaic arrays with different system configurations: literature review and field test results. *Solar Energy* **2003**, *74*, 217–233. doi:10.1016/S0038-092X(03)00155-5.
71. Pareek, S.; Dahiya, R. Enhanced power generation of partial shaded photovoltaic fields by forecasting the interconnection of modules. *Energy* **2016**, *95*, 561–572. doi:10.1016/j.energy.2015.12.036.
72. Belhaouas, N.; Cheikh, M.S.A.; Agathoklis, P.; Oularbi, M.R.; Amrouche, B.; Sedraoui, K.; Djilali, N. PV array power output maximization under partial shading using new shifted PV array arrangements. *Applied Energy* **2017**, *187*, 326–337. doi:10.1016/j.apenergy.2016.11.038.
73. Kurtz, B.; Kleissl, J. Measuring diffuse, direct, and global irradiance using a sky imager. *Solar Energy* **2016**. doi:10.1016/j.solener.2016.11.032.
74. Urquhart, B.; Kurtz, B.; Dahlin, E.; Ghonima, M.; Shields, J.E.; Kleissl, J. Development of a sky imaging system for short-term solar power forecasting. *Atmospheric Measurement Techniques* **2015**, *8*, 875–890. doi:10.5194/amt-8-875-2015.
75. Yang, H.; Kurtz, B.; Nguyen, D.; Urquhart, B.; Chow, C.W.; Ghonima, M.; Kleissl, J. Solar irradiance forecasting using a ground-based sky imager developed at UC San Diego. *Solar Energy* **2014**, *103*, 502–524. doi:10.1016/j.solener.2014.02.044.
76. Chauvin, R.; Nou, J.; Thil, S.; Grieu, S. Modelling the clear-sky intensity distribution using a sky imager. *Solar Energy* **2015**, *119*, 1–17. doi:10.1016/j.solener.2015.06.026.
77. Gohari, M.; Urquhart, B.; Yang, H.; Kurtz, B.; Nguyen, D.; Chow, C.; Ghonima, M.; Kleissl, J. Comparison of solar power output forecasting performance of the Total Sky Imager and the University of California, San Diego Sky Imager. *Energy Procedia* **2014**, *49*, 2340–2350. doi:10.1016/j.egypro.2014.03.248.
78. Schmidt, T.; Calais, M.; Roy, E.; Burton, A.; Heinemann, D.; Kilper, T.; Carter, C. Short-term solar forecasting based on sky images to enable higher PV generation in remote electricity networks. *Renewable Energy and Environmental Sustainability* **2017**, *2*, 23. doi:10.1051/rees/2017028.
79. Jazayeri, M.; Jazayeri, K.; Uysal, S. Generation of spatially dispersed irradiance time-series based on real cloud patterns. *Solar Energy* **2017**, *158*, 977–994. doi:10.1016/j.solener.2017.10.026.
80. Nou, J.; Chauvin, R.; Eynard, J.; Thil, S.; Grieu, S. Towards the intrahour forecasting of direct normal irradiance using sky-imaging data. *Heliyon* **2018**, *4*, e00598.
81. Anagnostos, D.; Schmidt, T.; Cavadias, S.; Soudris, D.; Poortmans, J.; Catthoor, F. A Method for Detailed, Short-Term Energy Yield Forecasting of Photovoltaic Installations. *Renewable Energy* **2018**. doi:10.1016/j.renene.2018.06.058.
82. Stein, J.S.; Hansen, C.W.; Reno, M.J. The variability index: A new and novel metric for quantifying irradiance and PV output variability. World Renewable Energy Forum. Citeseer, 2012, pp. 13–17.
83. Perpiñán, O.; Marcos, J.; Lorenzo, E. Electrical power fluctuations in a network of DC/AC inverters in a large PV plant: Relationship between correlation, distance and time scale. *Solar Energy* **2013**, *88*, 227–241. doi:10.1016/j.solener.2012.12.004.
84. Lenox, C.; Nelson, L. Variability comparison of large-scale photovoltaic systems across diverse geographic climates. Proceedings of the 25th European Photovoltaic Solar Energy Conference, Valencia, Spain, 2010.
85. Watanabe, T.; Oishi, Y.; Nakajima, T.Y. Characterization of surface solar-irradiance variability using cloud properties based on satellite observations. *Solar Energy* **2016**, *140*, 83–92. doi:10.1016/j.solener.2016.10.049.
86. Hummon, M.; Ibanez, E.; Brinkman, G.; Lew, D. Sub-Hour Solar Data for Power System Modeling From Static Spatial Variability Analysis: Preprint. Technical report, National Renewable Energy Laboratory (NREL), Golden, CO., 2012.
87. Wolff, B.; Kühnert, J.; Lorenz, E.; Kramer, O.; Heinemann, D. Comparing support vector regression for PV power forecasting to a physical modeling approach using measurement, numerical weather prediction, and cloud motion data. *Solar Energy* **2016**, *135*, 197–208. doi:10.1016/j.solener.2016.05.051.

88. Elsinga, B.; van Sark, W. Spatial power fluctuation correlations in urban rooftop photovoltaic systems. *Progress in Photovoltaics: Research and Applications* **2014**, pp. n/a–n/a. doi:10.1002/pip.2539.
89. Lonij, V.P.; Brooks, A.E.; Cronin, A.D.; Leuthold, M.; Koch, K. Intra-hour forecasts of solar power production using measurements from a network of irradiance sensors. *Solar Energy* **2013**, *97*, 58–66. doi:10.1016/j.solener.2013.08.002.
90. Mills, A. Implications of wide-area geographic diversity for short-term variability of solar power **2010**.
91. Munkhammar, J.; Widén, J. A Markov-chain probability distribution mixture approach to the clear-sky index. *Solar Energy* **2018**, *170*, 174–183. doi:10.1016/j.solener.2018.05.055.
92. Perez, R.; Hoff, T.; Kivalov, S. Spatial & temporal characteristics of solar radiation variability. Proceedings of the International Solar Energy (ISES) World Congress; , 2011.
93. Schwarz, M.; Folini, D.; Hakuba, M.Z.; Wild, M. Spatial representativeness of surface-measured variations of downward solar radiation: Spatiotemporal representativeness of SSR. *Journal of Geophysical Research: Atmospheres* **2017**. doi:10.1002/2017JD027261.
94. Bengulescu, M.; Blanc, P.; Wald, L. Characterizing Temporal Variability in Measurements of Surface Solar Radiation and its Dependence on Climate. *Energy Procedia* **2016**, *97*, 164–171. doi:10.1016/j.egypro.2016.10.045.
95. Bright, J.; Smith, C.; Taylor, P.; Crook, R. Stochastic generation of synthetic minutely irradiance time series derived from mean hourly weather observation data. *Solar Energy* **2015**, *115*, 229–242. doi:10.1016/j.solener.2015.02.032.
96. Hansen, C.W.; Stein, J.S.; Riley, D. Effect of time scale on analysis of PV system performance. *SANDIA Report* **2012**.
97. Lohmann, G.M.; Monahan, A.H. Effects of temporal averaging on short-term irradiance variability under mixed sky conditions. *Atmospheric Measurement Techniques* **2018**, *11*, 3131–3144. doi:10.5194/amt-11-3131-2018.
98. Kim, I. Markov chain Monte Carlo and acceptance–rejection algorithms for synthesising short-term variations in the generation output of the photovoltaic system. *IET Renewable Power Generation* **2017**, *11*, 878–888. doi:10.1049/iet-rpg.2016.0976.
99. Perry, M.; Troccoli, A. An approach for generating synthetic fine temporal resolution solar radiation time series from hourly gridded datasets. *Meteorologische Zeitschrift* **2017**, *26*, 265–276. doi:10.1127/metz/2016/0746.
100. Riley, D.M.; Cameron, C.P.; Jacob, J.A.; Granata, J.E.; Galbraith, G.M. Quantifying the effects of averaging and sampling rates on PV system and weather data. Photovoltaic Specialists Conference (PVSC), 2009 34th IEEE. IEEE, 2009, pp. 000456–000461.
101. Huang, J.; Davy, R.J. Predicting intra-hour variability of solar irradiance using hourly local weather forecasts. *Solar Energy* **2016**, *139*, 633–639. doi:10.1016/j.solener.2016.10.036.
102. Lave, M.; Weekley, A. Comparison of high-frequency solar irradiance: Ground measured vs. satellite-derived. Photovoltaic Specialists Conference (PVSC), 2016 IEEE 43rd. IEEE, 2016, pp. 1101–1106.
103. Hummon, M.; Weekley, A.; Searight, K.; Clark, K. Downscaling Solar Power Output to 4-seconds for Use in Integration Studies: Preprint. Technical report, National Renewable Energy Laboratory (NREL), Golden, CO., 2013.
104. Wegener, J.; Lave, M.; Luoma, J.; Kleissl, J. Temporal downscaling of irradiance data via hidden Markov models on wavelet coefficients: application to California solar initiative data. Technical report, 2012.
105. Kleissl, J. *Solar energy forecasting and resource assessment*; Academic Press, 2013.
106. Inman, R.H.; Pedro, H.T.; Coimbra, C.F. Solar forecasting methods for renewable energy integration. *Progress in Energy and Combustion Science* **2013**, *39*, 535–576. doi:10.1016/j.peccs.2013.06.002.
107. Graabak, I.; Korpås, M. Variability Characteristics of European Wind and Solar Power Resources—A Review. *Energies* **2016**, *9*, 449. doi:10.3390/en9060449.
108. Beyer, H.G. Handling of Small Scale Structures of the Irradiance Field for Solar Energy System Analysis – A Review. *Energy Procedia* **2016**, *97*, 141–148. doi:10.1016/j.egypro.2016.10.039.
109. Badescu, V.; Gueymard, C.A.; Cheval, S.; Oprea, C.; Baciu, M.; Dumitrescu, A.; Iacobescu, F.; Milos, I.; Rada, C. Computing global and diffuse solar hourly irradiation on clear sky. Review and testing of 54 models. *Renewable and Sustainable Energy Reviews* **2012**, *16*, 1636–1656. doi:10.1016/j.rser.2011.12.010.

110. Gueymard, C.A. Clear-sky irradiance predictions for solar resource mapping and large-scale applications: Improved validation methodology and detailed performance analysis of 18 broadband radiative models. *Solar Energy* **2012**, *86*, 2145–2169. doi:10.1016/j.solener.2011.11.011.
111. Reno, M.J.; Hansen, C.W.; Stein, J.S. Global horizontal irradiance clear sky models: Implementation and analysis. *SANDIA report SAND2012-2389* **2012**.
112. Lefèvre, M.; Oumbe, A.; Blanc, P.; Espinar, B.; Gschwind, B.; Qu, Z.; Wald, L.; Schroedter-Homscheidt, M.; Hoyer-Klick, C.; Arola, A.; Benedetti, A.; Kaiser, J.W.; Morcrette, J.J. McClear: a new model estimating downwelling solar radiation at ground level in clear-sky conditions. *Atmospheric Measurement Techniques* **2013**, *6*, 2403–2418. doi:10.5194/amt-6-2403-2013.
113. Dumortier, D. *Modelling global and diffuse horizontal irradiances under cloudless skies with different turbidities; Daylight II*, JOU2-CT92-0144, Final Report, 1995.
114. Macke, A.; Seifert, P.; Baars, H.; Barthlott, C.; Beekmans, C.; Behrendt, A.; Bohn, B.; Brueck, M.; Bühl, J.; Crewell, S.; Damian, T.; Deneke, H.; Düsing, S.; Foth, A.; Di Girolamo, P.; Hammann, E.; Heinze, R.; Hirsikko, A.; Kalisch, J.; Kalthoff, N.; Kinne, S.; Kohler, M.; Löhnert, U.; Madhavan, B.L.; Maurer, V.; Muppa, S.K.; Schween, J.; Serikov, I.; Siebert, H.; Simmer, C.; Späth, F.; Steinke, S.; Träumner, K.; Trömel, S.; Wehner, B.; Wieser, A.; Wulfmeyer, V.; Xie, X. The HD(CP)2 Observational Prototype Experiment (HOPE) – an overview. *Atmos. Chem. Phys.* **2017**, *17*, 4887–4914. doi:10.5194/acp-17-4887-2017.
115. Schade, N.H.; Macke, A.; Sandmann, H.; Stick, C. Enhanced solar global irradiance during cloudy sky conditions. *Meteorologische Zeitschrift* **2007**, *16*, 295–303. doi:10.1127/0941-2948/2007/0206.
116. Piacentini, R.D.; Salum, G.M.; Fraidenraich, N.; Tiba, C. Extreme total solar irradiance due to cloud enhancement at sea level of the NE Atlantic coast of Brazil. *Renewable Energy* **2011**, *36*, 409–412. doi:10.1016/j.renene.2010.06.009.
117. Pecenak, Z.K.; Mejia, F.A.; Kurtz, B.; Evan, A.; Kleissl, J. Simulating irradiance enhancement dependence on cloud optical depth and solar zenith angle. *Solar Energy* **2016**, *136*, 675–681. doi:10.1016/j.solener.2016.07.045.
118. Gueymard, C.A. Cloud and albedo enhancement impacts on solar irradiance using high-frequency measurements from thermopile and photodiode radiometers. Part 1: Impacts on global horizontal irradiance. *Solar Energy* **2017**, *153*, 755–765. doi:10.1016/j.solener.2017.05.004.
119. Tovar, J.; Olmo, F.J.; Alados-Arboledas, L. One-minute global irradiance probability density distributions conditioned to the optical air mass. *Solar Energy* **1998**, *62*, 387–393.
120. Olseth, J.A.; Skartveit, A. A probability density model for hourly total and beam irradiance on arbitrarily orientated planes. *Solar Energy* **1987**, *39*, 343–351.
121. Ripley, B.D. *Modern applied statistics with S*; Springer, 2002.
122. Friedrich, R.; Peinke, J.; Sahimi, M.; Reza Rahimi Tabar, M. Approaching complexity by stochastic methods: From biological systems to turbulence. *Physics Reports* **2011**, *506*, 87–162.
123. M.S. Nikulin (originator). Three-sigma rule. In *Encyclopedia of Mathematics*; 2002.
124. Woyte, A.; Richter, M.; Moser, D.; Mau, S.; Reich, N.; Jahn, U. Monitoring of photovoltaic systems: good practices and systematic analysis. Proc. 28th European Photovoltaic Solar Energy Conference, 2013, pp. 3686–3694.
125. Ngoko, B.; Sugihara, H.; Funaki, T. Synthetic generation of high temporal resolution solar radiation data using Markov models. *Solar Energy* **2014**, *103*, 160–170. doi:10.1016/j.solener.2014.02.026.
126. Hansen, C.W.; Stein, J.S.; Ellis, A. Simulation of one-minute power output from utility-scale photovoltaic generation systems. Technical Report SAND 2011-5529, Sandia National Laboratories, 2011.
127. Morf, H. The stochastic two-state solar irradiance model (STSIM). *Solar Energy* **1998**, *62*, 101–112.
128. Morf, H. A stochastic solar irradiance model adjusted on the Ångström–Prescott regression. *Solar Energy* **2013**, *87*, 1–21. doi:10.1016/j.solener.2012.10.005.
129. Pfenninger, S. Energy scientists must show their workings. *Nature News* **2017**, *542*, 393.
130. Perpiñán, O. Statistical analysis of the performance and simulation of a two-axis tracking PV system. *Solar Energy* **2009**, *83*, 2074–2085. doi:10.1016/j.solener.2009.08.008.
131. Gueymard, C.A.; Ruiz-Arias, J.A. Extensive worldwide validation and climate sensitivity analysis of direct irradiance predictions from 1-min global irradiance. *Solar Energy* **2016**, *128*, 1–30. doi:10.1016/j.solener.2015.10.010.

132. Engerer, N. Minute resolution estimates of the diffuse fraction of global irradiance for southeastern Australia. *Solar Energy* **2015**, *116*, 215–237. doi:10.1016/j.solener.2015.04.012.
133. Lohmann, G.M. Solar irradiance variability on small spatial and temporal scales. Dissertation, Carl von Ossietzky Universität Oldenburg, Oldenburg, Germany, 2017.